2D Materials

PAPER

Tunable broadband light emission from graphene

RECEIVED
24 November 2020

REVISED
4 March 2021

ACCEPTED FOR PUBLICATION
19 March 2021

PUBLISHED
3 May 2021

Lavinia Ghirardini[1,8], Eva A A Pogna[1,2,8], Giancarlo Soavi[3,4,8], Andrea Tomadin[5], Paolo Biagioni[1], Stefano Dal Conte[1], Sandro Mignuzzi[3], Domenico De Fazio[3], Takashi Taniguchi[6], Kenji Watanabe[7], Lamberto Duò[1], Marco Finazzi[1], Marco Polini[5], Andrea C Ferrari[3,*], Giulio Cerullo[1,*] and Michele Celebrano[1,*]

[1] Politecnico di Milano, Physics Department, Piazza Leonardo Da Vinci 32, 20133 Milano, Italy
[2] NEST, CNR-NANO and Scuola Normale Superiore, Piazza San Silvestro 12, Pisa I-56127, Italy
[3] Cambridge Graphene Centre, University of Cambridge, 9 JJ Thomson Avenue, Cambridge CB3 0FA, United Kingdom
[4] Institute of Solid State Physics, Friedrich Schiller University Jena, Max-Wien Platz 1, Jena 07743, Germany
[5] Physics Department, Pisa University, Largo Bruno Pontecorvo 3, 56127 Pisa, Italy
[6] International Center for Materials Nanoarchitectonics, National Institute for Materials Science, 1-1 Namiki, Tsukuba 305-0044, Japan
[7] Research Center for Functional Materials, National Institute for Materials Science, 1-1 Namiki, Tsukuba 305-0044, Japan
[8] These authors equally contributed to this work.
[*] Authors to whom any correspondence should be addressed.

E-mail: michele.celebrano@polimi.it, giulio.cerullo@polimi.it and acf26@eng.cam.ac.uk

Keywords: graphene, hot photoluminescence, out of equilibrium electrons, hyperbolic phonons, electron-phonon cooling, third-harmonic generation

Abstract

Graphene is an ideal material for integrated nonlinear optics thanks to its strong light–matter interaction and large nonlinear optical susceptibility. It has been used in optical modulators, saturable absorbers, nonlinear frequency converters, and broadband light emitters. For the latter application, a key requirement is the ability to control and engineer emission wavelength and bandwidth, as well as electronic temperature. Here, we demonstrate that the emission wavelength of graphene's broadband hot carrier photoluminescence can be tuned by integration in photonic cavities, while thermal management can be achieved by out-of-plane heat transfer to hexagonal boron nitride. Our results pave the way to graphene-based ultrafast broadband light emitters with tunable emission.

1. Introduction

The opto-electronic properties of graphene [1] are ideal for a variety of applications [2], such as optical modulators [3–5], saturable absorbers [6], plasmonic devices [7, 8], and various types of broadband detectors [9], working from the THz [10] to the visible (VIS)/infrared (IR) [11–13]. Despite being atomically thin, single–layer graphene (SLG) absorbs 2.3% per layer in the VIS (400–750 nm) [14] and near-IR (NIR, 1000–2400 nm) [15], and has a large nonlinear optical response (e.g. third order nonlinear susceptibility $\chi^{(3)} \sim 10^{-19}$–10^{-16} m^2 V^{-2} in the VIS and NIR depending on excitation photon energy and doping [16, 17]), paving the way to new applications, such as gate-tunable frequency converters [16–18] and broadband light–emitters [19–27].

In intrinsic SLG, due to the absence of a gap and the linear dispersion of conduction and valence bands around the Dirac points, the massless Dirac fermions have a spectrally flat optical response [14, 15, 28]. In principle, the gapless nature of SLG along with the ultrafast charge carrier recombination are expected to inhibit radiative recombination [19], while blackbody radiation can still occur due to intra-band radiative transitions, figure 1(a). Nevertheless, broadband light emission from excited charge carriers, i.e. hot carrier photoluminescence (HotPL), can be achieved in SLG via radiative recombination of hot electrons (HEs) [19, 20, 29] characterized by a nonequilibrium thermal distribution [16, 17, 30]. A key feature of SLG-based thermal emitters is the broad emission at room-temperature, which can be extended from THz [31] to VIS [24], by tuning the HEs temperature, T_e. An out-of-equilibrium distribution of electrons can be induced both by electrical [24–27] and ultrafast (∼100 fs) optical [19–21] excitation. Electrically driven HotPL emission can be controlled by current pulse duration [32] and SLG channel dimension [27]. SLG can sustain high current densities (up to

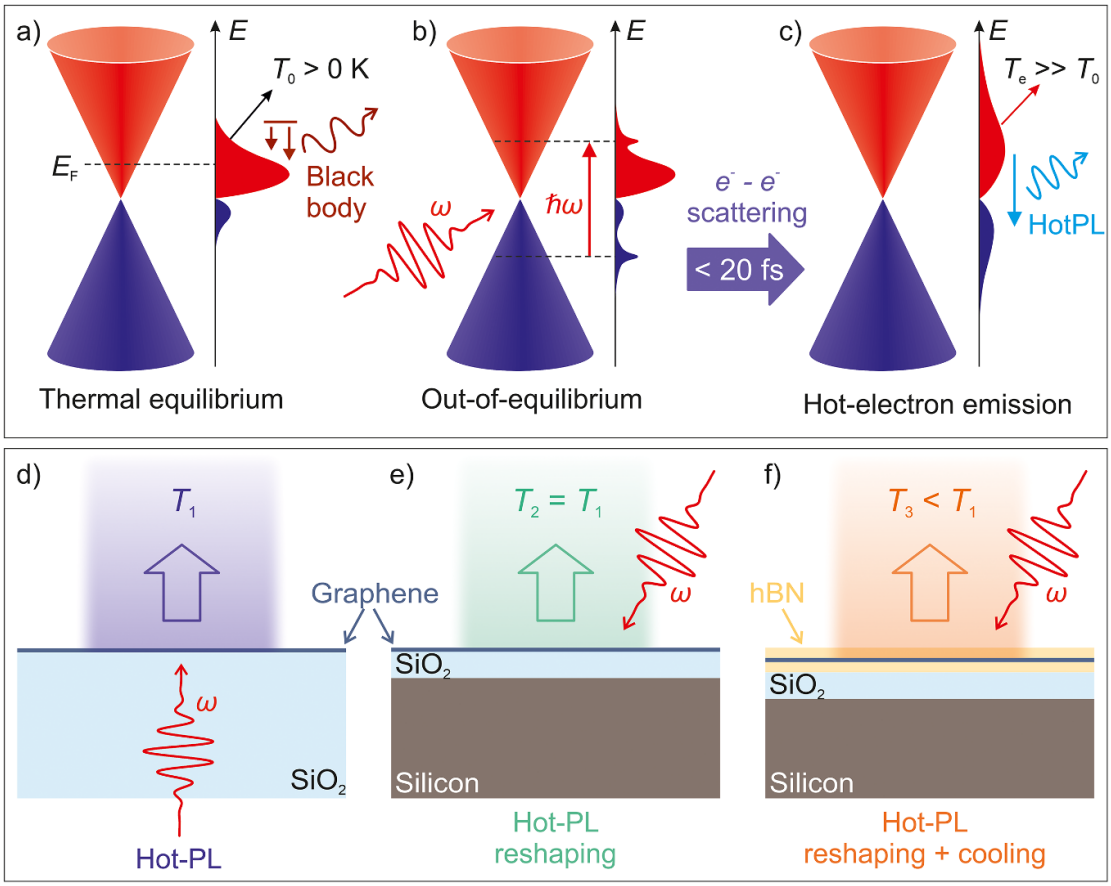

Figure 1. HotPL emission mechanism and tuning principles. (a)–(c) Sketches of *n*-doped SLG conical bands in the vicinity of the Dirac points and of e (red)/hole (h,blue) density distribution (i.e. the e/h distribution multiplied by the density of states), at various stages of the photoexcited HotPL dynamics. (a) The electron density distribution intrinsic broadening for $T_0 > 0$ K causes black-body emission in SLG. (b) Upon ultrafast laser excitation, out-of-equilibrium charge distributions are formed on sub-20 fs time scales. (c) At time scales comparable with our pulse duration the e distribution thermalizes, resulting in $T_e \gg T_0$ and in two different chemical potentials for e/h. The increased h density in the valence band compared to the equilibrium situation (a) allows for the HE radiative recombination, leading to photoluminescence emission (HotPL). (d) HotPL emission upon ultrafast laser excitation in SLG on SiO_2 at $T_e = T_1 \gg T_0$. (e) The same process in SLG on SiO_2/Si at the same $T_e = T_2 = T_1$ is spectrally reshaped by cavity effects. (f) HotPL is further tuned when SLG is encapsulated in a double layer of hBN, thanks to the cooling effects between HE and hyperbolic phonons in hBN, which lead to $T_e = T_3 < T_1$.

$\sim 10^8$ A cm^{-2}) [26] and reaches high ($\sim 10^8$ A cm^{-2}) saturation current density [21, 24]. However, in SLG on SiO_2/Si the heat dissipation to the substrate limits the achievable T_e (up to 600 K [21], corresponding to an emission spectrum spanning mid-IR and NIR). Using suspended architectures, it is possible to reach higher T_e (up to 2880 K [24]), thus VIS emission. Manipulation of the thermal emission spectrum in SLG was obtained exploiting interference in trench structures [24], integration into a dielectric optical cavity [26], using frequency-selective metasurfaces [33] and sub-wavelength photonic crystals [27]. Photoexcitation with femtosecond pulses produces high $T_e > 1000$ K [16, 19], corresponding to emission extended to the VIS range (up to 3.5 eV) [16, 17, 19, 34].

Following ultrafast-light absorption by vertical transitions within the Dirac cones, electrons (e) are brought in a out of equilibrium distribution (see figure 1(b)), which thermalizes via e-e scattering in a very short time (<20 fs) [34] into a hot Fermi Dirac distribution (i.e. a thermal distribution) with T_e that can reach 2000–3000 K [16, 17, 19, 34], figure 1(c). The HEs then thermalize with the lattice on a ps timescale [35, 36], via emission of optical and acoustic phonons [35–37]. Due to the short lifetime of HEs in SLG [35, 36], thermal emission via HotPL has the advantage of enabling ultra-fast modulation comparable to the inverse of the HEs recombination time ($\sim$1 ps) [26, 36]. Modulation frequencies up to THz could in principle be achieved, and up to tens of GHz were experimentally reported in SLG [26]. This makes SLG-based light emitters promising for on-chip light sources in high-speed (GHz–THz) communication and as alternative to lasers and LEDs in Si photonics [3, 5]. SLG-based devices hold promise also in gas sensing [38, 39], where state of the art devices exploit thermal emitters based on micro-electro-mechanical systems (MEMS) [38], which feature modulation frequencies $\sim$100 Hz [38]. In this framework, absorption enhancement, e.g. by integration of SLG in optical cavities [40]

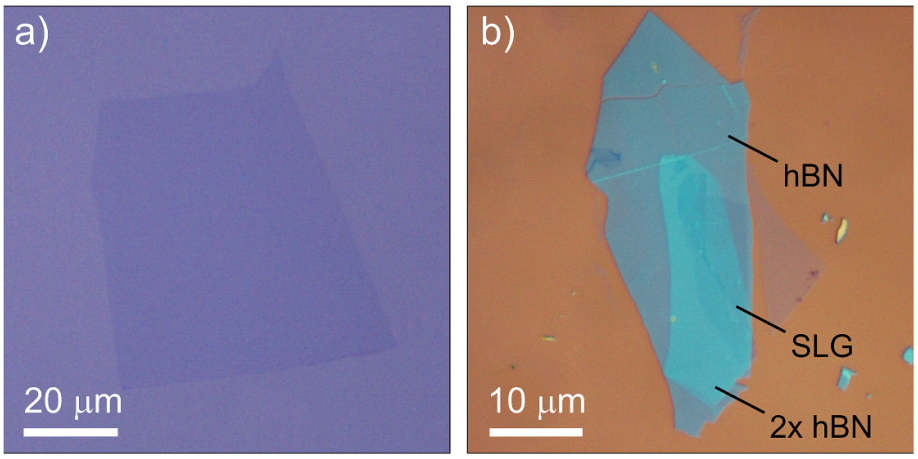

Figure 2. Microscope images of representative samples. (a) MC-SLG. (b) hBN/SLG/hBN. SLG on the right side of the image is embedded between wider (on top) and smaller (on the bottom) 10 nm thick hBN flakes.

or photonic crystals [41], constitutes a promising route to increase emissivity. This strategy, previously demonstrated with thermal emitters based on nanostructures [42], MEMS [39] and quantum wells [43], can mitigate the low ($\sim 4.5 \times 10^{-3}$) efficiency (i.e. ratio between optically radiated and applied electrical power) of thermal emitters based on SLG [24]. In the IR, gate-tunable absorption > 90% was reported in SLG-based thermal emitters embedded in photonic cavities [44, 45], suggesting that an emissivity close to one could be achieved [44, 45].

Here we investigate the nonlinear light emission of SLG, following NIR excitation with 150 fs pulses at 1554 nm (0.8 eV). We show emission wavelength and bandwidth tuning of the HotPL, modulated by both photonic cavity effects and T_e engineering, figures 1(d)–(f). To this aim, we compare samples produced by micromechanical cleavage (MC) of bulk crystals [46], both pristine (MC-SLG) and encapsulated (hBN/SLG/hBN) in two ∼10 nm-thick layers of hexagonal Boron Nitride (hBN) transferred on a 285 nm-thick SiO_2 layer on Si, with SLG grown by chemical vapor deposition (CVD-SLG), transferred either on SiO_2/Si or on glass. This allows us to simultaneously investigate the effects of substrate, defects and T_e on the SLG HotPL. The HotPL spectral emission profile is reshaped by photonic cavity effects induced by the substrate (see figure 1(e)), as confirmed by a model describing the SLG HotPL combining finite difference time domain (FDTD) simulations, accounting for the substrate photonic response, with a semiclassical expression for the emission spectrum. We also demonstrate, through both HotPL and third harmonic generation (THG) measurements, that hBN allows to further tune the HotPL emission, thanks to the cooling process occurring between hyperbolic phonons in hBN and SLG HE, figure 1(f). Our approach can describe the incoherent emission from any layered material (LM) coupled to any substrate and optical environment, and is thus relevant for the design of photonic devices based on LMs.

2. Results and discussion

2.1. Fabrication and characterization of SLG devices

CVD-SLG is grown on Cu as described in Ref. [47]. A Cu foil (99.8% pure) is placed in a furnace and annealed at 1000 °C in a 20 standard cubic centimeters per minute (sccm) hydrogen flux at ∼196 mTorr for 30 min. The growth is initiated by adding 5 sccm CH_4 for 30 min. SLG is then transferred on 200 μm-thick SiO_2 coverslips or 285 nm-thick SiO_2 on Si by polymer–assisted Cu wet etching [47], using polymethyl methacrylate. Direct growth on SiO_2/Si would not have allowed to obtain SLG with low defects density [48, 49]. Flakes of hBN and SLG are also prepared by MC [46] of bulk graphite (NGS Naturgraphit) and hBN using adhesive tape. hBN crystals are grown at high pressure and high temperature conditions, as described in Ref. [50]. SLG and hBN flakes are identified prior to transfer by a combination of optical microscopy [51] and Raman spectroscopy [52–55]. We use ∼10 nm-thick hBN flakes as they provide sufficient screening from charge impurities in the underlying substrate [56, 57].

Figure 2 shows representative microscope images of MC-SLG and hBN/SLG/hBN samples.

The Raman spectra of all samples, measured with a Renishaw Raman inVia spectrometer equipped with a 50× objective at 514 nm, are in figure 3. The orange curve shows the Raman spectrum of SLG on Cu before transfer, after subtraction of the PL from Cu [58]. This has a single sharp Lorentzian 2D peak with full width at half maximum FWHM(2D) ∼ 33 cm^{-1} and peak position Pos(2D) ∼ 2710 cm^{-1}, a fingerprint of SLG [53]. The D peak is negligible. In hBN/SLG/hBN, the hBN E_{2g} Raman peak is

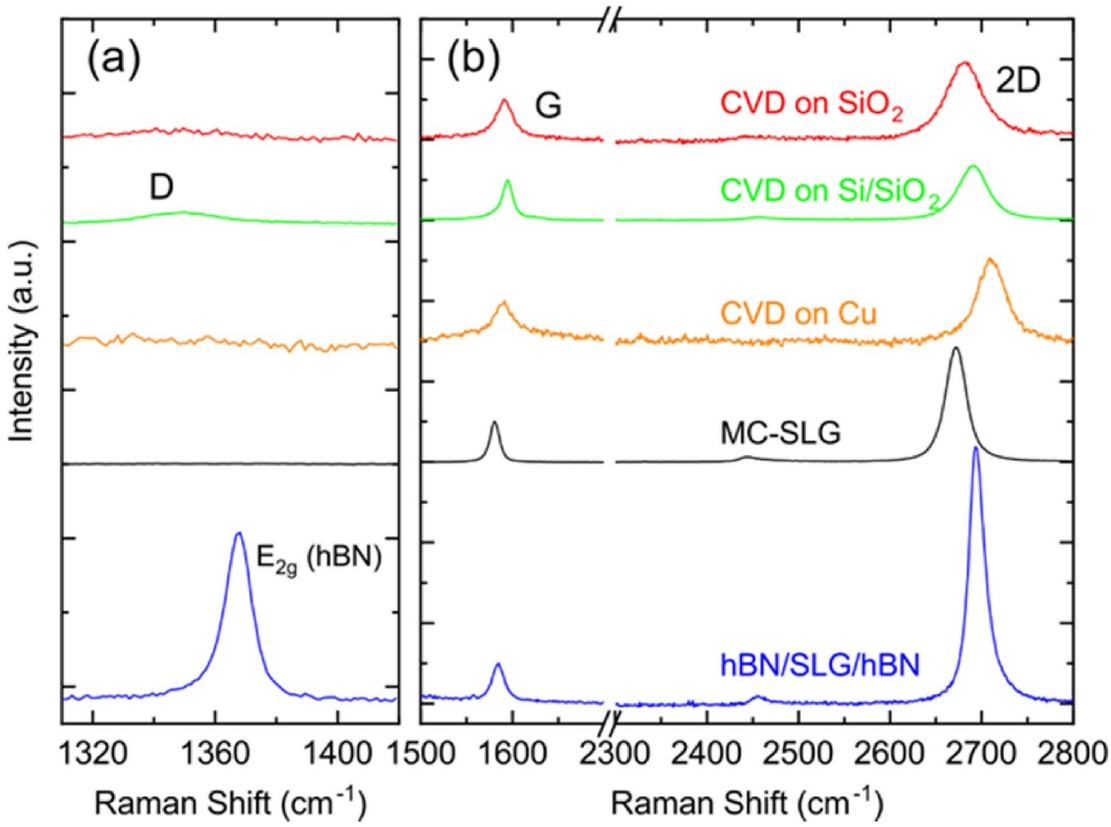

Figure 3. Raman spectra of SLG samples at 514 nm excitation. All spectra in (a) and (b) are normalized to the G peak intensity.

a combination of those from both top and bottom hBN. This yields a single peak with position Pos(E_{2g}) $\sim$ 1367 cm^{-1} and FWHM(E_{2g}) $\sim$ 9.8 cm^{-1}, as expected for bulk hBN [52, 54].

Table 1 summarizes the Raman fit parameters and the resulting Fermi energy, E_F, carrier concentration, n, doping type (n or p), strain, and defect density, n_D. E_F is estimated from A(2D)/A(G), I(2D)/I(G) (A peak area and I peak intensity) and FWHM(G) [59, 60], while strain is estimated from Pos(G) [61, 62]. Biaxial strain can be differentiated from uniaxial by the absence of G-peak splitting with increasing strain, however at low ($\lesssim$0.5%) strain the splitting cannot be resolved. For uniaxial(biaxial) strain, Pos(G) shifts by $\sim$23(60)cm^{-1}/% [61, 62]. Since Pos(G) depends on both E_F and strain [59, 61], to get the contribution of strain only, we first derive E_F from A(2D)/A(G), I(2D)/I(G) and FWHM(G), which are independent on strain [59, 60, 63], and then calculate Pos(G) corresponding this E_F. The strain is then retrieved from the difference between the experimental and calculated Pos(G). The strain values in table 1 are positive (negative) for tensile (compressive) strain. The doping type is estimated from Pos(2D), which decreases from p to n [59]. Note that Pos(2D) shifts by $\sim$83(191) cm^{-1}/% with uniaxial (biaxial) strain [61]. We thus calculate the contribution of strain to Pos(2D) and subtract this from the experimental Pos(2D) to obtain the doping type. n_D is estimated from I(D)/I(G) and E_F [64, 65]. The error bars in table 1 are calculated from the standard error of the fits, the spectrometer resolution ($\sim$1 cm^{-1}) and the uncertainty associated with the methods to estimate E_F from Pos(G), FWHM(G), I(2D)/I(G), A(2D)/A(G) and Pos(2D).

To verify the optical uniformity and spatial homogeneity of the samples, THG maps are acquired using a nonlinear optical microscope equipped with a 0.85 numerical aperture (NA) air objective for both IR illumination, with 150 fs pulses at 1554 nm from an Er-doped fiber laser, and light collection. The power impinging on the samples ranges from 300 to 700 μW (pump fluence $\sim$2.1–4.9 J m^{-2}). The sample is mounted upside-down on a piezo stage to acquire nonlinear emission spatial maps in reflection, deflected to the detection path by a dichroic mirror (cut-off wavelength $\sim$1000 nm), to reject the residual laser radiation. A flip mirror allows selecting between a VIS-NIR spectrometer, to record the whole emission spectrum, and a Si-based single photon avalanche detector (SPAD) for THG detection. For THG measurements a narrow-band filter (NBF, with central wavelength 520 nm (2.4 eV), and bandwidth 40 nm (0.18 eV)) is in front of the SPAD. All samples are excited from the air side. THG maps are acquired by imaging 80 $\times$ 80 μm^2 areas on the SLG edge to enable

Table 1. Please ROTATE TABLE 90 degrees and put horizontal at full page width Raman peaks fit parameters and corresponding E_F, doping concentration n, and defects density n_D, with associated error (±).

Sample	Pos(G) (cm^{-1})	FWHM(G) (cm^{-1})	Pos(2D) (cm^{-1})	FWHM(2D) (cm^{-1})	A(2D)/A(G)	I(2D)/I(G)	I(D)/I(G)	E_F(meV)	Doping type	n ($\times 10^{12}$) (cm^{-2})	Uniaxial strain (%)	Biaxial strain (%)	n_D ($\times 10^{10}$) (cm^{-2})
CVD-SLG on SiO_2	1591.2 ± 1	22.7 ± 1	2681 ± 1	45.1 ± 1	4.09 ± 0.06	2.06 ± 0.02	0.14 ± 0.01	300 ± 80	*n*	5.5 ± 2.8	−0.13 ± 0.13	−0.05 ± 0.04	6.6 ± 1.0
CVD-SLG on Si/SiO_2	1594.5 ± 1	14.2 ± 1	2690.4 ± 1	36.9 ± 1	3.8 ± 0.03	1.45 ± 0.01	0.17 ± 0.01	260 ± 140	*n*	4.9 ± 4	−0.24 ± 0.20	−0.09 ± 0.07	6.9 ± 2.2
MC-SLG on Si/SiO_2	1580.8 ± 1	11.3 ± 1	2672 ± 1	25.2 ± 1	6.37 ± 0.05	2.86 ± 0.02	0.012 ± 0.001	180 ± 30	*n*	1.9 ± 0.6	0.12 ± 0.03	0.04 ± 0.01	0.3 ± 0.1
hBN/SLG/hBN on Si/SiO_2	1584.5 ± 1	14.8 ± 1	2694.7 ± 1	19.9 ± 1	9.32 ± 0.17	6.95 ± 0.08	0.04 ± 0.01	90 ± 50	*p*	0.6 ± 0.7	−0.03 ± 0.03	−0.01 ± 0.01	0.5 ± 0.5

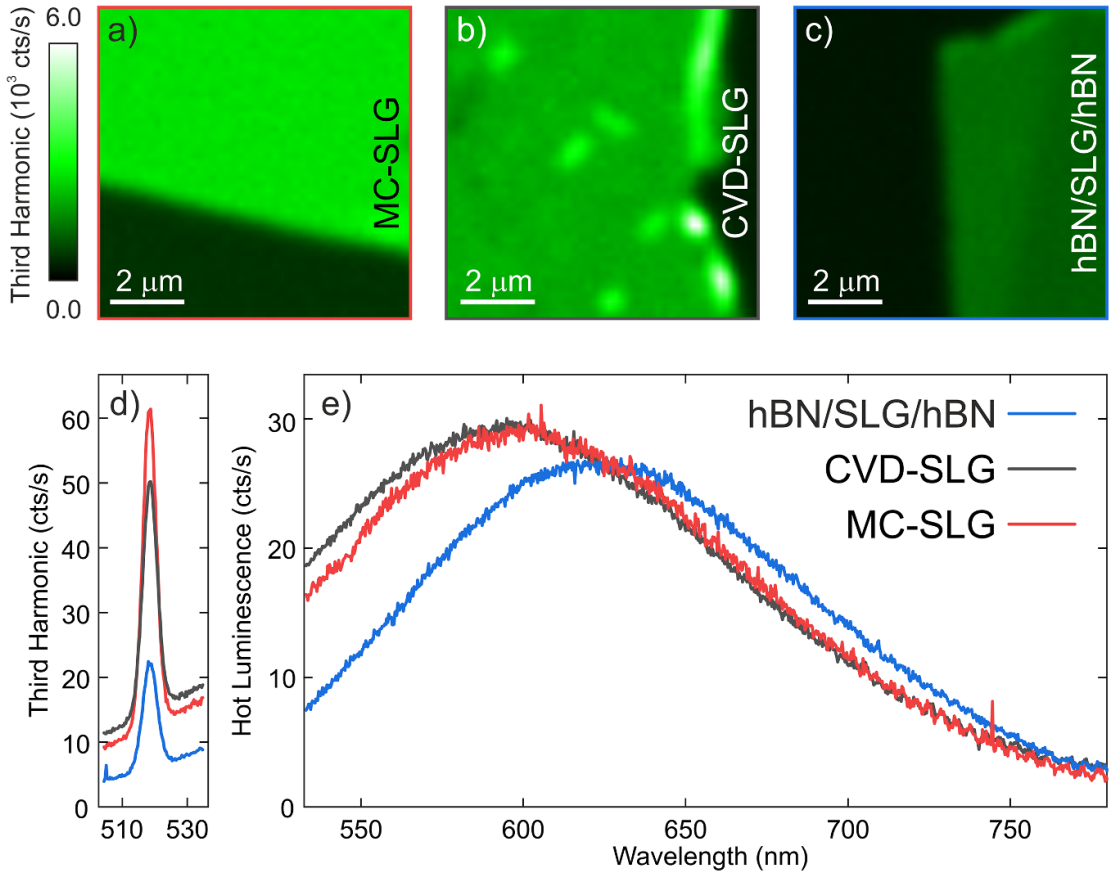

Figure 4. THG maps for (a) MC-SLG, (b) CVD-SLG, and (c) hBN/SLG/hBN on SiO_2/Si. The scanned region is 10 × 10 μm^2. (d) THG peaking at ∼518 nm for MC-SLG (red), CVD-SLG (gray) and hBN/SLG/hBN (blue). (e) The VIS-NIR portion of the spectrum, between 500 and 800 nm, showing HotPL spectra.

simultaneous recording of the SiO_2 signal as a background to be subtracted from the total signal collected on SLG.

Figures 4(a)–(c) show 10 × 10 μm^2 areas of the overall THG maps for MC-SLG on SiO_2/Si (figure 4(a)), CVD-SLG on SiO_2/Si (figure 4(b)), and hBN/SLG/hBN on SiO_2/Si (figure 4(c)). The THG and PL emission from the bare SiO_2/Si (darker areas in the maps) are about one order of magnitude lower than the SLG signal in the spectral window set by the filter. The THG conversion efficiency, defined as $\eta^{THG} = I_{3\omega}/I_\omega$ [16], where I_ω and $I_{3\omega}$ are the incident and THG power, respectively, is calculated by computing the total number of photons emitted at the peak fluence ∼4.9 J m^{-2} (700 μW), about a factor two below the damage threshold of SLG (∼10 J m^{-2}) for 150 fs pump pulses with a repetition rate ∼80 MHz. The damage threshold is defined as the fluence at which the THG signal degrades after a 1 min irradiation.

The total absolute THG emitted power is estimated by taking into account the overall transmission efficiency of our setup and evaluating the collected fraction of the THG power. We model the emission from SLG as that of a dipole parallel to the substrate using FDTD simulations [66]. We estimate an overall photon collection efficiency within the objective NA of ∼20% for SLG on SiO_2/Si, and ∼10% for hBN/SLG/hBN on SiO_2/Si. The drop in collection efficiency at the THG wavelength for hBN/SLG/hBN on SiO_2/Si is due to presence of the 2 hBN layers, which redirect half of the THG out of the collection NA (see figure 5). This, together with the objective transmission at the THG wavelength (∼80%), the optical throughput in the detection path (∼20%), the single-photon avalanche detector quantum yield (∼50%) and its filling factor (∼50%), determines a drop by over two orders of magnitude in the number of detected photons with respect to the emitted ones. Thus, $I_{3\omega}$ is ∼160, 130, 45 fW for MC-SLG, CVD-SLG and hBN/SLG/hBN, respectively, for an average I_ω ∼ 700 μW. This defines higher-bound values for $\eta^{THG} \sim 2.3 \times 10^{-10}$, 1.8×10^{-10} and 1.3×10^{-10} for the three samples, respectively, in agreement with our previous measurements [16, 17]. η^{THG} decreases going from MC-SLG to CVD-SLG, to hBN/SLG/hBN. In general, η^{THG} depends on T_e, E_F, I_ω, and on the incident photon energy $\hbar\omega$ [16]. Since I_ω and $\hbar\omega$ are the same in all measurements and for all samples, we attribute the different η^{THG} to variations of T_e and E_F.

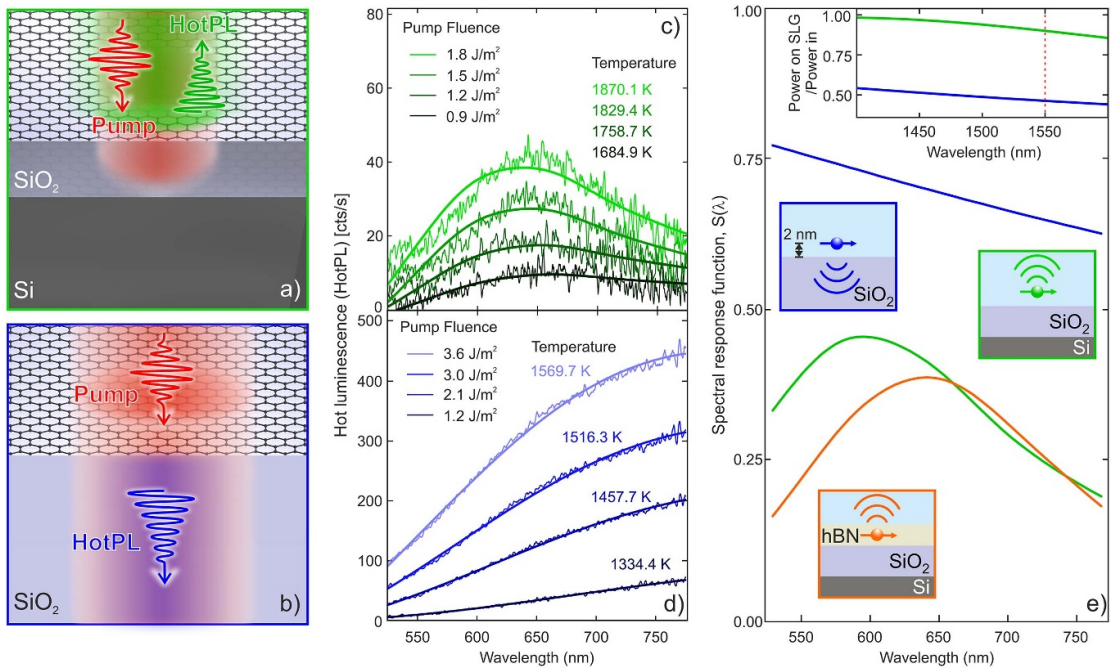

Figure 5. Sketches of CVD SLG on (a) SiO_2/Si and (b) infinitely thick SiO_2. Ultrafast pump pulses (red) arrive from the top using a 0.7 NA objective in both configurations, while HotPL (green and blue in a and b, respectively) is collected in back-reflection through the same objective in (a) and in transmission through a 0.85 NA objective in (b). (c), (d) HotPL spectra (thin lines) and fits (thick lines) from CVD-SLG for the configurations sketched in (a) and (b), respectively. The fits are obtained from equation (1) by adjusting T_e, ξ and δ. ξ is (c) ∼100 and (d) ∼4000. δ varies between −5 and −16 cts s^{-1} depending on the impinging fluence. (e) $S(\lambda)$ is calculated for the various substrates using a dipole located 2 nm above SiO_2/Si (light green, middle inset), SiO_2 (blue, top inset) and inside a double layer of hBN (orange, bottom inset). Inset: pump power ratio impinging on the SLG as a function of wavelength for SiO_2 (blue) and SiO_2/Si (green), calculated by dividing the effective power deposited on SLG due to the presence of the substrate with that exiting the objective.

2.2. Reshaping of HotPL emission with a photonic cavity

To further investigate the effect of the photonic environment on the nonlinear emission properties of SLG, we record the nonlinear emission spectra from each sample with an integration time of 10 s, while raster-scanning over 10 × 10 μm^2. This is done to minimize photodamage and suppress the influence of intensity hot-spots resulting from nonlinear field enhancements associated with defects [67]. The substrate nonlinear emission, evaluated in a similar way, features mostly ambient light coming from non-perfect shielding of the spectrometer, along with an extremely weak (∼2 orders of magnitude lower than the HotPL signal) multi–photon PL coming from SiO_2 [68]. While they cannot be employed for calibration, the background spectra are subtracted to obtain clean HotPL and THG spectra.

The emission spectra in figures 4(d) and (e) show a THG peak ∼518 nm (∼2.4 eV) which corresponds to one third of the 1554 nm wavelength of the pump beam, as expected for this nonlinear process [69]. The HotPL signal arising from photoexcited HEs in SLG gives a broad feature in the 500–800 nm spectral range. Refs. [19, 20, 29, 34] reported ultrafast HotPL in MC SLG both on mica and Si/SiO_2 for 800 nm (1.55 eV) excitation, showing an exponential decay at increasing photon energies. A similar behavior was seen in electroluminescence [24], and modeled within a semi-classical approach to account for out-of-equilibrium conditions [24]. The HotPL spectra in figure 3(e) show instead a maximum between 600 nm (2.06 eV) and 700 nm (1.77 eV), depending on sample and pump fluence. We attribute this behavior, which qualitatively differs from those reported in Refs. [19, 20, 25, 34], to the different excitation photon energy and sample geometry. The SiO_2 thickness (285 nm) is comparable with the VIS and NIR wavelengths (400–1000 nm). Such thin-film interference effects are key to make graphene and related materials visible on substrates [70].

To investigate the spectral reshaping of the HotPL emission from SLG, we compare the emission from two CVD SLG samples deposited on different substrates: SiO_2/Si or a 200 μm SiO_2 coverslip (see figures 5(a) and (b)). In the second case, the spectrum is acquired by adapting the setup in figure 2 to collect light in transmission. To efficiently collect the nonlinear emission, mostly directed towards the glass substrate, we insert a 0.85 NA air objective at the opposite side of the sample with respect to the illumination objective, as illustrated in figure 5(b). The collected light is then redirected to the same detection path. The background-subtracted HotPL spectra from CVD-SLG on SiO_2/Si and SiO_2, as a

function of pump fluence, are in figure 5(c) (green) and figure 5(d) (blue), respectively.

To model the data, we first numerically estimate how the photonic environment reshapes the HotPL spectrum emitted by SLG. This is done by considering the emission from an electric dipole placed 2 nm above the substrate (either a semi-infinite glass plane or a thin SiO_2/Si film). The dipole is oriented parallel to the substrate surface and its emission within the NA of the collection objective is evaluated with FDTD. This gives a set of spectral response functions, $S(\lambda)$, for the different substrates (figure 4(e)). For a semi-infinite SiO_2 the spectral response is almost flat in the investigated wavelength range (blue line), while the emission is significantly reshaped for SiO_2/Si (light green line), which acts as a broadband photonic cavity.

We apply a similar approach to evaluate the reshaping effect for hBN/SLG/hBN. In this case, the simulated emitting dipole is inserted in the center of a 20 nm hBN slab with refractive index $n = 2.17$ [71, 72]. hBN shifts the position of the dipole with respect to the SiO_2/Si photonic cavity, resulting in a red shift of the emission peak (orange line in figure 5(e)).

Semiclassical PL theories yield the profile of the emitted light, but not the overall intensity [19], as the latter depends on the interaction between e and quantized modes of the electromagnetic spectrum. Fully-quantized theories [73] require the integration of quantum-mechanical equations of motion with sub-femtosecond accuracy. This is a substantial computational effort, given that HotPL is emitted for several hundreds fs after pulsed excitation [19, 20]. Following the pump pulse, the instantaneous intensity of the HotPL decreases in time, due to electron–hole (e–h) recombination and the cooling of the HE distribution. However, the time-integrated spectrum is dominated by the signal produced by the thermalized e distribution at its hottest temperature, i.e. at the end of the pump pulse.

Although a full quantum treatment of the out-of-equilibrium system would be required, here we approximate it by the signal emitted by HEs immediately after photoexcitation. We express the collected HotPL intensity as the product of $S(\lambda)$ and a factor proportional to the SLG joint density of states (JDOS) at the emitted photon wavelength for a thermalized e–h distribution at T_e [24]:

$$I(\lambda, T_e) = S(\lambda) \cdot \xi \frac{2hc^2}{\lambda^5} \frac{1}{\left[e^{\left(\frac{hc}{2\lambda k_B T_e}\right)} + 1\right]^2} + \delta. \quad (1)$$

In equation (1), $\xi \frac{2hc^2}{\lambda^5} \frac{1}{\left[e^{\left(\frac{hc}{2\lambda k_B T_e}\right)}+1\right]^2}$ is the JDOS multiplied by the Boltzmann distribution [24], through the dimensionless coefficient ξ. This depends on the oscillator strength of the direct transitions in the Dirac cones [24], parametrizing the overall intensity of the HotPL spectrum, integrated in time between pulses. Equation (1) is a reliable model for the HotPL in SLG as long as T_e is the same for both electrons and holes and the photoexcited carrier density is much larger than the SLG doping [16, 74], as in our case. In equation (1), h is the Planck constant, c the speed of light in vacuum, k_B the Boltzmann constant, and λ the wavelength. δ [cts s^{-1}] is a constant introduced to correct for residual offsets after background subtraction. For short wavelengths ($\lambda \ll \frac{hc}{2k_B T_e}$), the dominating term in equation (1) is an exponential tail, similar to that obtained, in such a spectral range, from blackbody emission [19]. The fits using equation (1) are superimposed to the data in figure 4(c) (solid green lines) and figure 4(d) (solid blue lines) for CVD-SLG on Si/SiO_2 and SiO_2, respectively. T_e is treated as an independent parameter. A univocal set of values for ξ and δ is used for each sample to attain the best fit. These values are allowed to vary for the different samples, since they depend on several experimental conditions (e.g. sample mounting, small deviations in optical setup alignment and background level). Our model allows to account for the variation of HotPL intensity with pump intensity through T_e, without need for further normalization. The HotPL intensity is a nonlinear function of the pump intensity through T_e, while ξ is a constant proportionality factor that accounts for the experimental conditions, such as setup collection efficiency.

In both CVD-SLG samples T_e increases with pump fluence. Although the pump fluences for CVD-SLG on SiO_2/Si are lower than for CVD-SLG on SiO_2, the corresponding T_e is higher in the first case. This can be ascribed to the influence of the photonic cavity created by SiO_2/Si on the 1554 nm pump beam which, as confirmed by FDTD (inset of figure 5(e)), enhances the pump fluence by a factor ~2. The agreement between model and experiments for both data sets validates our approach.

2.3. Tuning the HotPL emission by out-of-plane heat transfer

To demonstrate the possibility of engineering the HotPL via out-of-plane heat transfer, we investigate with our model the HotPL emission of three different samples: MC-SLG, CVD-SLG and hBN/SLG/hBN. Figures 6(a)–(c) plot the HotPL spectra as a function of incident fluence, accounting for the enhancement induced by the substrate (see inset in figure 5(e)). For each sample, all spectra are fitted using equation (1) and optimizing T_e, ξ and δ. While ξ is not sensitive to fluence, δ changes with it. This could be ascribed to an imperfect background compensation. The excellent agreement between model and experiments demonstrates the robustness of this approach, once the photonic environment and the substrate are accounted for. The fluence-dependent T_e plots in

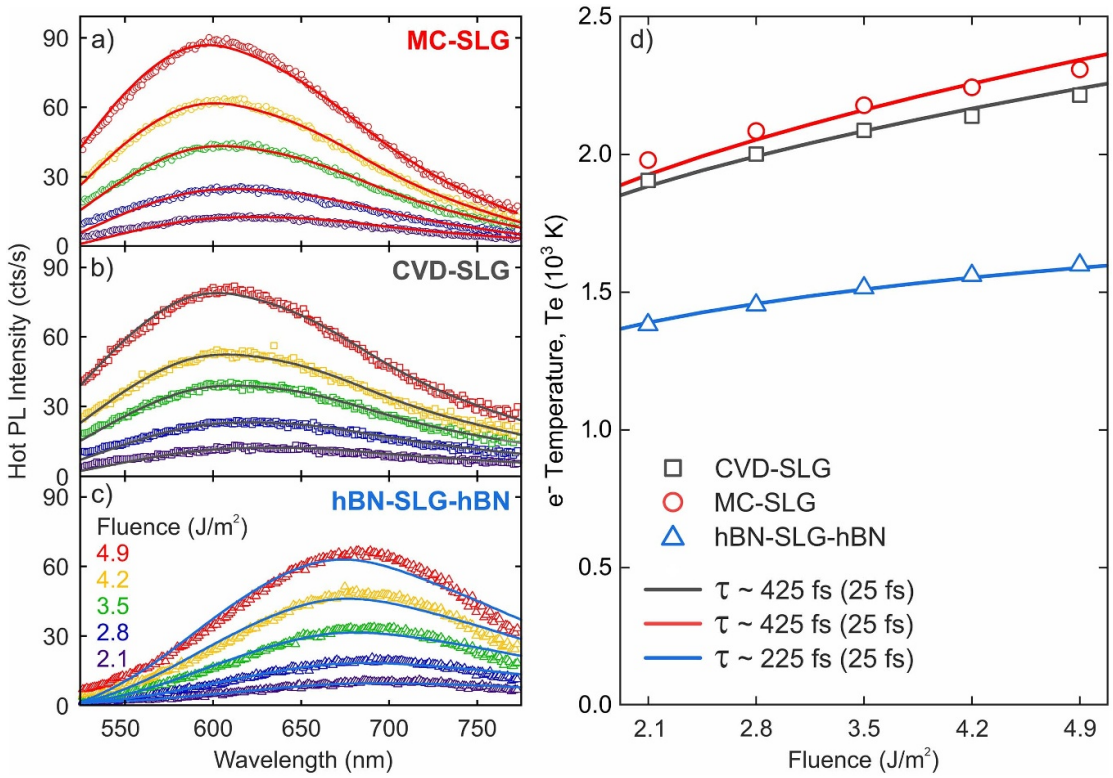

Figure 6. (a)–(c) Fluence-dependent HotPL for (a) MC-SLG, (b) CVD-SLG and (c) hBN/SLG/hBN and fits from equation (1). The spectra in (a)–(c) are collected using pump fluencies $\sim$ 2.1 (violet), 2.8 (blue), 3.5 (green), 4.2 (yellow), 4.9 J m^{-2} (red), the same as in (d). (d) Fluence-dependence of T_e extracted from the fits. (a)–(c) also show the fits for MC-SLG (solid red line), CVD-SLG (solid gray line) and hBN/SLG/hBN (solid light blue line), obtained varying δ from -7 to -34 cts s^{-1}. ξ provides the best fits for values of 25 (MC-SLG and CVD-SLG) and 800 (hBN/SLG/hBN). The solid lines represent T_e from the model in Refs. [16, 17]. τ is searched on a mesh with a step of 25 fs, which sets the fit uncertainty.

figure 6(d) show that MC- and CVD-SLG reach a similar $T_e \sim$ 2200–2300 K for a pump fluence $\sim$4.9 J m^{-2}, consistent with the T_e reported in Refs. [16, 19]. Despite small deviations, which we ascribe to different E_F, the observation of similar T_e for the same illuminating fluence implies that the fabrication process and E_F do not significantly affect the electron dynamics and the nonlinear optical response in our experimental conditions. The data are integrated over the whole emission decay time [19], while the calculations consider only the emission in the instant of time when T_e is the highest.

For hBN/SLG/hBN a significant drop in T_e is observed (see figure 6(d)), as reflected in the red-shift of the emission spectrum (see figure 6(c)), which can only be partially attributed to the photonic response of hBN/SLG/hBN (orange curve in figure 5(e)), which is different from that on bare SiO_2/Si (green curve in figure 5(e)). The almost 2-fold reduction in T_e calls for further underlying physical processes associated with SLG encapsulation in hBN. In hBN/SLG/hBN, out-of-plane heat transfer can occur between SLG and hBN thanks to near-field coupling between SLG HEs and the hyperbolic phonons in hBN [75, 76]. This offers an efficient cooling channel, associated with a significant reduction of the SLG HE lifetime [77, 75, 76].

Therefore, the overall red shift in the SLG HotPL caused by the encapsulation with hBN can be interpreted as due to the combination of two effects: (a) a purely photonic one, associated with the presence of the two high refractive index hBN layers that produce an emission spectral reshaping; (b) a more fundamental one, consisting in the modification of the thermal properties of HEs in SLG by the presence of the heat-sink consisting in the near-field coupling to hyperbolic phonons in hBN. Although a lower T_e can be related to the observed HotPL red-shift (figures 5(a)–(c)), the quantitative evaluation of T_e can be done only if the photonic response of the whole heterostructure is considered.

To further support these observations, we estimate the expected T_e using the model of Refs.[78, 79], based on a set of rate equations for T_e and the photoexcited carrier density in SLG, solved in the steady-state regime. Dissipation is accounted for in the relaxation-time approximation, parametrized by a cooling time τ. The absorption coefficient α [80] includes a saturable, T_e-dependent, contribution, due to inter-band vertical transitions [6], and a residual, nonsaturable, constant contribution α_{res} [81]. α_{res} corresponds to a 'residual' absorbance in the Pauli-blocked regime [81]. In the case of non-encapsulated

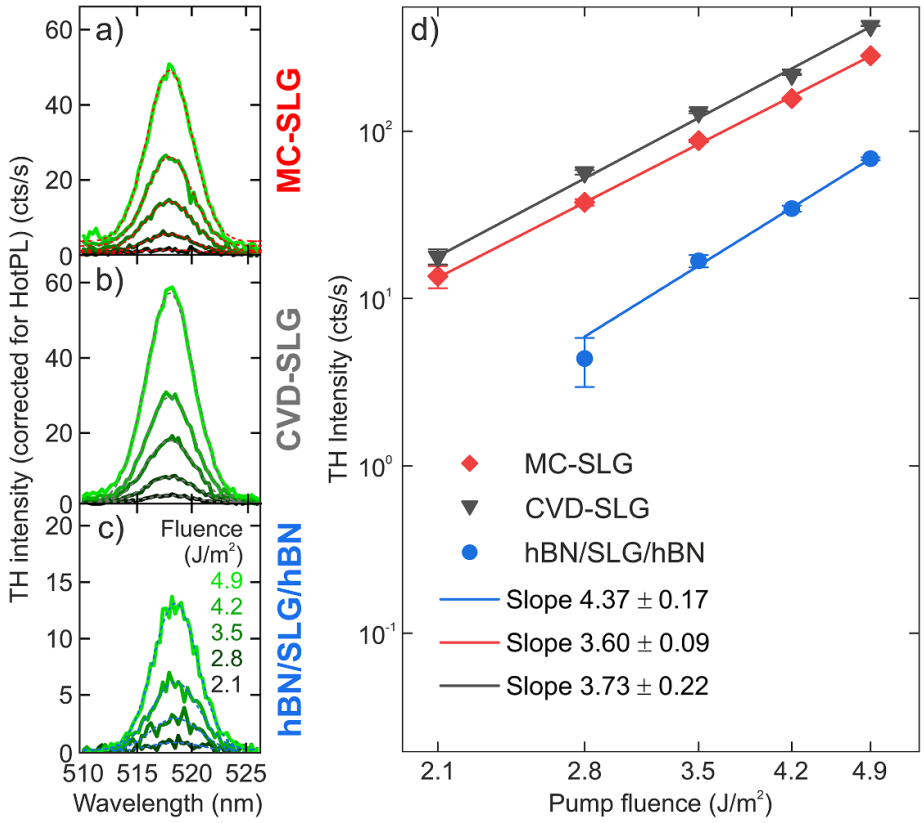

Figure 7. Fluence dependence of TH generation. Fluence dependent TH spectra of (a) MC-SLG, (b) CVD-SLG and (c) hBN/SLG/hBN after subtraction of HotPL background. The red, gray and blue dashed lines are Gaussian fits. (d) TH powers, measured as the areas under the Gaussian curves in panels (a)–(c), as a function of pump fluence. Solid lines are fits with power law curves.

SLG, this is of the same order of magnitude as the nonsaturable absorption $\alpha_{NS} \sim 0.8\%$ [6]. We apply this model to fit the T_e dependence on the illumination fluence, finding $\tau \sim 425$ fs for CVD- and MC-SLG, and ~ 225 fs for hBN/SLG/hBN. The uncertainty in the determination of τ is dictated by the mesh step of 25 fs in our model.

This shorter relaxation time can be ascribed to the coupling with the hBN hyperbolic phonons. We also find $\alpha_{res} \sim 0.08\%$ for hBN/SLG/hBN, and a larger $\alpha_{res} \sim 0.4\%$, 0.5% for CVD and MC-SLG, respectively. We use in the model a single T_e for both HEs and hot h, since we assume the time-integrated spectra to be dominated by the signal produced by the thermalized e distribution at its highest T_e, i.e. at the end of pump pulse. Therefore, the model describes the steady state of the carriers under the action of heating, due to the pump pulse, and cooling, due to coupling with phonons.

2.4. THG dependence on T_e in SLG

We explore the impact of the different E_F and T_e on THG emission, by comparing the THG fluence dependence in the three samples. After subtracting the HotPL contribution from the nonlinear emission spectra, we obtain the THG spectra in figures 7(a)–(c). The fluence-dependent wavelength-integrated THG powers, plotted in log-log scale in figure 7(d), reveals a slope that exceeds the expected 3 [69], in agreement with Ref. [17], where we reported a sizable deviation from the typical cubic power law for THG caused by the dependence of the nonlinear susceptibility on both T_e and E_F. In our experiments, E_F ~0.3 eV for CVD-SLG, ~0.18 eV for MC-SLG and ~0.09 eV for hBN/SLG/hBN (see table 1), hence E_F is much smaller than the pump photon energy (~0.8 eV). This condition makes the THG process extremely sensitive to T_e. As we discussed in Ref. [17], for $E_F < h\nu/2$, η^{THG} is expected to grow with T_e, therefore resulting in a power law with an exponent >3. The lower T_e in hBN/SLG/hBN is accompanied by a higher THG power slope, compared to the other samples, in good agreement with our model in Ref. [16]. In particular, as we discussed in the supplementary information of Ref. [16], the strongest variation of η^{THG} upon increasing photoexcitation fluence is expected for $T_e < 1800$ K and $E_F/h\nu \ll 1$, which overlap the working conditions identified for the hBN/SLG/hBN sample. The THG signal from hBN/SLG/hBN is reduced by a factor ~2, when compared to that of MC-SLG and CVD-SLG, due to cavity effects (see figure 5(e)). However, this does not affect the slope in figure 7, hence the evaluation of the effects of T_e on η^{THG}.

3. Conclusions

We measured the broadband light emission of different graphene samples following ultrashort pulse excitation. We modelled the spectra by combining the emission from an out-of-equilibrium HE bath and the photonic environment of graphene, also taking the response of the collection optics into account. We found that both substrate (via photonic cavity effects) and T_e increase contribute to shaping the HotPL emission, as well as the THG efficiency. We derived the dependence of T_e on incident fluence. Under similar illumination conditions, hBN-encapsulated graphene (hBN/SLG/hBN) shows a substantially lower T_e than the other samples, due to the coupling of SLG HEs with hBN hyperbolic phonons. T_e influences also the dependence of the emitted third harmonic intensity on pump fluence, giving a power law with exponent >3 [17]. Thus, in SLG, both incoherent (HotPL) and coherent (THG) emission are extremely sensitive to T_e. This must be considered in ultrafast all-optical applications of SLG-based devices, such as tunable broadband light emitters and nonlinear frequency converters. Our results clarify the interplay between HEs and optical nonlinear effects in graphene, and can be used to tailor the emission wavelength and temperature of graphene-based high-speed broadband light emitters. Our approach can be extended to reproduce the incoherent emission from any LM coupled to any substrate.

Data availability statement

The data that support the findings of this study are available upon reasonable request from the authors.

Acknowledgments

We acknowledge funding from the EU Graphene and Quantum Flagships, ERC Grants Hetero2D, GSYNCOR, EPSRC Grant Nos. EP/N010345/1, EP/L016087/1, the Elemental Strategy Initiative conducted by the MEXT, Japan, Grant Nos. JPMXP0112101001, JSPS KAKENHI Grant No. JP20H00354 and the CREST(JPMJCR15F3), JST, the German Research Foundation DFG (CRC 1375 NOA project number B5) and the Daimler and Benz foundation.

ORCID iDs

Eva A A Pogna https://orcid.org/0000-0003-4779-3549
Giancarlo Soavi https://orcid.org/0000-0003-2434-2251
Kenji Watanabe https://orcid.org/0000-0003-3701-8119
Marco Finazzi https://orcid.org/0000-0002-9197-3654
Andrea C Ferrari https://orcid.org/0000-0003-0907-9993
Michele Celebrano https://orcid.org/0000-0003-3336-3580

References

[1] Ferrari A C *et al* 2015 Science and technology roadmap for graphene, related two-dimensional crystals, and hybrid systems *Nanoscale* **7** 4598–810
[2] Bonaccorso F, Sun Z, Hasan T and Ferrari A C 2010 Graphene photonics and optoelectronics *Nat. Photon.* **4** 611–22
[3] Romagnoli M, Sorianello V, Midrio M, Koppens F H L, Huyghebaert C, Neumaier D, Galli P, Templ W, D'Errico A and Ferrari A C 2018 Graphene-based integrated photonics for next-generation datacom and telecom *Nat. Rev. Mater.* **3** 392–414
[4] Liu M, Yin X, Ulin-Avila E, Geng B, Zentgraf T, Ju L, Wang F and Zhang X 2011 A graphene-based broadband optical modulator *Nature* **474** 64–7
[5] Sorianello V, Midrio M, Contestabile G, Asselberghs I, Van Campenhout J, Huyghebaert C, Goykhman I, Ott A K, Ferrari A C and Romagnoli M 2018 Graphene-silicon phase modulators with gigahertz bandwidth *Nat. Photon.* **12** 40–4
[6] Sun Z, Hasan T, Torrisi F, Popa D, Privitera G, Wang F, Bonaccorso F, Basko D M and Ferrari A C 2010 Graphene mode-locked ultrafast laser *ACS Nano* **4** 803–10
[7] Grigorenko A N, Polini M and Novoselov K S 2012 Graphene plasmonics *Nat. Photon.* **6** 749–58
[8] Koppens F H L, Chang D E and García De Abajo F J 2011 Graphene plasmonics: a platform for strong light–matter interactions *Nano Lett.* **118** 3370–7
[9] Koppens F H L, Mueller T, Avouris P, Ferrari A C F, Vitiello M S and Polini M 2014 Photodetectors based on graphene, other two-dimensional materials and hybrid systems *Nat. Nanotechnol.* **9** 780–93
[10] Vicarelli L, Vitiello M S, Coquillat D, Lombardo A, Ferrari A C, Knap W, Polini M, Pellegrini V and Tredicucci A 2012 Graphene field-effect transistors as room-temperature terahertz detectors *Nat. Mater.* **11** 865–71
[11] Mueller T, Xia F and Avouris P 2010 Graphene photodetectors for high-speed optical communications *Nat. Photon.* **4** 297–301
[12] Goykhman I *et al* 2016 On-chip integrated, silicon–graphene plasmonic Schottky photodetector with high responsivity and avalanche photogain *Nano Lett.* **16** 3005–13
[13] De Fazio D *et al* 2016 High responsivity, large-area graphene/MoS_2 flexible photodetectors *ACS Nano* **10** 8252–62
[14] Nair R R, Blake P, Grigorenko A N, Novoselov K S, Booth T J, Stauber T, Peres N M R and Geim A K 2008 Fine structure constant defines visual transparency of graphene *Science* **320** 1308
[15] Mak K F, Sfeir M Y, Wu Y, Lui C H, Misewich J A and Heinz T F 2008 Measurement of the optical conductivity of graphene *Phys. Rev. Lett.* **101** 196405
[16] Soavi G *et al* 2018 Broadband, electrically tunable third-harmonic generation in graphene *Nat. Nanotechnol.* **13** 583–8
[17] Soavi G *et al* 2019 Hot electrons modulation of third-harmonic generation in graphene *ACS Photonics* **6** 2841–9
[18] Jiang T *et al* 2018 Gate-tunable third-order nonlinear optical response of massless Dirac fermions in graphene *Nat. Photon.* **12** 430–6
[19] Lui C H, Mak K F, Shan J and Heinz T F 2010 Ultrafast photoluminescence from graphene *Phys. Rev. Lett.* **105** 127404

[20] Liu W-T, Wu S W, Schuck P J, Salmeron M, Shen Y R and Wang F 2010 Nonlinear broadband photoluminescence of graphene induced by femtosecond laser irradiation *Phys. Rev.* B **82** 081408(R)
[21] Freitag M, Chiu H-Y, Steiner M, Perebeinos V and Avouris P 2010 Thermal infrared emission from biased graphene *Nat. Nanotechnol.* **5** 497–501
[22] Chen C-F *et al* 2011 Controlling inelastic light scattering quantum pathways in graphene *Nature* **471** 617–20
[23] Li T, Luo L, Hupalo M, Zhang J, Tringides M C, Schmalian J and Wang J 2012 Femtosecond population inversion and stimulated emission of dense Dirac fermions in graphene *Phys. Rev. Lett.* **108** 167401
[24] Kim Y D *et al* 2015 Bright visible light emission from graphene *Nat. Nanotechnol.* **10** 676
[25] Huang D *et al* 2018 Gate switching of ultrafast photoluminescence in graphene *Nano Lett.* **18** 7985–90
[26] Kim Y D *et al* 2018 Ultrafast graphene light emitters *Nano Lett.* **18** 934–40
[27] Shiue R-J, Gao Y, Tan C, Peng C, Zheng J, Efetov D K, Kim Y D, Hone J and Englund D 2019 Thermal radiation control from hot graphene electrons coupled to a photonic crystal nanocavity *Nat. Commun.* **10** 109
[28] Mak K F, Ju L, Wang F and Heinz T F 2012 Optical spectroscopy of graphene: from the far infrared to the ultraviolet *Solid State Commun.* **152** 1341–9
[29] Handloser M, Piredda G, Lombardo A, Ferrari A C and Hartschuh A 2011 Non-linear photoluminescence from graphene *OSA Technical Digest* pp JSII1–2
[30] Castro Neto A H, Guinea F, Peres N M R, Novoselov K S and Geim A K 2009 The electronic properties of graphene *Rev. Mod. Phys.* **81** 109
[31] Bahk Y-M, Ramakrishnan G, Choi J, Song H, Choi G, Kim Y H, Ahn K J, Kim D-S and Planken P C M 2014 Plasmon enhanced terahertz emission from single layer graphene *ACS Nano* **8** 9089
[32] Miyoshi Y, Fukazawa Y, Amasaka Y, Reckmann R, Yokoi T, Ishida K, Kawahara K, Ago H and Maki H 2018 High-speed and on-chip graphene blackbody emitters for optical communications by remote heat transfer *Nat. Commun.* **9** 1279
[33] Shi C, Mahlmeister N H, Luxmoore I J and Nash G R 2018 Metamaterial-based graphene thermal emitter *Nano Res.* **11** 3567–73
[34] Stöhr R J, Kolesov R, Pflaum J and Wrachtrup J 2010 Fluorescence of laser-created electron-hole plasma in graphene *Phys. Rev.* B **82** 121408(R)
[35] Breusing M, Kuehn S, Winzer T, Malić E, Milde F, Severin N, Rabe J P, Ropers C, Knorr A and Elsaesser T 2011 Ultrafast nonequilibrium carrier dynamics in a single graphene layer *Phys. Rev.* B **83** 153410
[36] Sun D, Wu Z-K, Divin C, Li X, Berger C, De Heer W A, First P N and Norris T B 2008 Ultrafast relaxation of excited Dirac fermions in epitaxial graphene using optical differential transmission spectroscopy *Phys. Rev. Lett.* **101** 157402
[37] Lazzeri M, Piscanec S, Mauri F, Ferrari A C and Robertson J 2005 Electron transport and hot phonons in carbon nanotubes *Phys. Rev. Lett.* **95** 236802
[38] Lawton L M, Mahlmeister N H, Luxmoore I J and Nash G R 2014 Prospective for graphene based thermal mid-infrared light emitting devices *AIP Adv.* **4** 087139
[39] Lochbaum A, Fedoryshyn Y, Dorodnyy A, Koch U, Hafner A and Leuthold J 2017 On-chip narrowband thermal emitter for mid-IR optical gas sensing *ACS Photon.* **4** 1371–80
[40] Safei A, Chandra S, Leuenberger M N and Chanda D 2019 Wide angle dynamically tunable enhanced infrared absorption on large-area nanopatterned graphene *ACS Nano* **13** 421–8
[41] Gu T, Petrone N, McMillan J F, Van Der Zande A, Yu M, Lo G Q, Kwong D L, Hone J and Wong C W 2012 Regenerative oscillation and four-wave mixing in graphene optoelectronics *Nat. Photon.* **6** 554–9
[42] Inoue T, De Zoysa M, Asano T and Noda S 2015 Realization of narrowband thermal emission with optical nanostructures *Optica* **2** 27
[43] Inoue T, De Zoysa M, Asano T and Noda S 2013 Single-peak narrow-bandwidth mid-infrared thermal emitters based on quantum wells and photonic crystals *Appl. Phys. Lett.* **102** 191110
[44] Thongrattanasiri S, Koppens F H L and De Abajo J G 2012 Complete optical absorption in periodically patterned graphene *Phys. Rev. Lett.* **108** 047401
[45] Fan Y, Liu Z, Zhang F, Zhao Q, Wei Z, Fu Q, Li J, Gu C and Li H 2015 Tunable mid-infrared coherent perfect absorption in a graphene meta-surface *Sci. Rep.* **5** 13956
[46] Novoselov K S, Jiang D, Schedin F, Booth T J, Khotkevich V V, Morozov S V and Geim A K 2005 Two-dimensional atomic crystals *Proc. Natl Acad. Sci. USA* **102** 10451
[47] Li X *et al* 2009 Large-area synthesis of high-quality and uniform graphene films on copper foils *Science* **324** 1312–4
[48] Bonaccorso F, Lombardo A, Hasan T, Sun Z, Colombo L and Ferrari A C 2012 Production and processing of graphene and 2d crystals *Mater. Today* **15** 564–89
[49] Backes C *et al* 2020 Production and processing of graphene and related materials *2D Mater.* **7** 022001
[50] Taniguchi T and Watanabe K 2007 Synthesis of high-purity boron nitride single crystals under high pressure by using Ba–BN solvent *J. Cryst. Growth* **303** 525–9
[51] Casiraghi C, Hartschuh A, Lidorikis E, Qian H, Harutyunyan H, Gokus T, Novoselov K S and Ferrari A C 2007 Rayleigh imaging of graphene and graphene layers *Nano Lett.* **7** 2711–7
[52] Reich S, Ferrari A C, Arenal R, Loiseau A, Bello I and Robertson J 2005 Resonant Raman scattering in cubic and hexagonal boron nitride *Phys. Rev.* B **71** 205201
[53] Ferrari A C *et al* 2006 Raman spectrum of graphene and graphene layers *Phys. Rev. Lett.* **97** 187401
[54] Arenal R, Ferrari A C, Reich S, Wirtz L, Mevellec J-Y, Lefrant S, Rubio A and Loiseau A 2006 Raman spectroscopy of single-wall boron nitride nanotubes *Nano. Lett.* **6** 1812–6
[55] Purdie D G, Pugno N M, Taniguchi T, Watanabe K, Ferrari A C and Lombardo A 2018 Cleaning interfaces in layered materials heterostructures *Nat. Commun.* **9** 5387
[56] Hong X, Zou K and Zhu J 2009 Quantum scattering time and its implications on scattering sources in graphene *Phys. Rev.* B **80** 241415
[57] Burson K M, Cullen W G, Adam S, Dean C R, Watanabe K, Taniguchi T, Kim P and Fuhrer M S 2013 Direct imaging of charged impurity density in common graphene substrates *Nano Lett.* **13** 3576–80
[58] Lagatsky A A *et al* 2013 2 μm solid-state laser mode-locked by single-layer graphene *Appl. Phys. Lett.* **102** 013113
[59] Das A *et al* 2008 Monitoring dopants by Raman scattering in an electrochemically top-gated graphene transistor *Nat. Nanotechnol.* **3** 210–5
[60] Basko D M, Piscanec S and Ferrari A C 2009 Electron-electron interactions and doping dependence of the two-phonon Raman intensity in graphene *Phys. Rev.* B **80** 165413
[61] Mohiuddin T M G *et al* 2009 Uniaxial strain in graphene by Raman spectroscopy: G peak splitting, Grüneisen parameters, and sample orientation *Phys. Rev.* B **79** 205433
[62] Yoon D, Son Y-W and Cheong H 2011 Strain-dependent splitting of the double-resonance Raman scattering band in graphene *Phys. Rev. Lett.* **106** 2011
[63] Pisana S, Lazzeri M, Casiraghi C, Novolesov K S, Geim A K and Ferrari A C 2007 Breakdown of the adiabatic Born–Oppenheimer approximation in graphene *Nat. Mater.* **6** 198–201
[64] Bruna M, Ott A K, Ijäs M, Yoon D, Sassi U and Ferrari A C 2014 Doping dependence of the Raman spectrum of defected graphene *ACS Nano* **8** 7432–41

[65] Cançado L G, Jorio A, Martins Ferreira E H, Stavale F, Achete C A, Capaz R B, Moutinho M V O, Lombardo A, Kulmala T S and Ferrari A C 2011 Quantifying defects in graphene via Raman spectroscopy at different excitation energies *Nano Lett.* **11** 3190–6
[66] Sullivan D M 2013 *Electromagnetic Simulation Using the FDTD Method* 2nd edn (Hoboken, NJ: Wiley)
[67] Bozhevolnyi S I, Beermann J and Coello V 2003 Direct observation of localized second-harmonic enhancement in random metal nanostructures *Phys. Rev. Lett.* **90** 197403
[68] Baraban A P, Samarin S N, Prokofiev V A, Dmitriev V A, Selivanov A A and Petrov Y 2019 Luminescence of SiO_2 layers on silicon at various types of excitation *J. Lumin.* **205** 102–8
[69] Boyd R 2008 *Nonlinear Optics* 3rd edn (New York: Academic)
[70] Casiraghi C, Pisana S, Novoselov K S, Geim A K and Ferrari A C 2007 Rayleigh Imaging of Graphene and Graphene Layers *Nano Lett.* **7** 2711–7
[71] Schubert M, Rheinlander B, Franke E, Neumann H, Hann J, Order M and Richter F 1997 Anisotropy of boron nitride thin-film reflectivity spectra by generalized ellipsometry *Appl. Phys. Lett.* **70** 1819
[72] Rah Y, Jin Y, Kim S and Yu K 2019 Optical analysis of the refractive index and birefringence of hexagonal boron nitride from the visible to near-infrared *Opt. Lett.* **44** 3797–800
[73] Kira M and Koch S W 2012 *Semiconductor Quantum Optics* (Cambridge: Cambridge University Press)
[74] Tomadin A *et al* 2018 The ultrafast dynamics and conductivity of photoexcited graphene at different Fermi energies *Sci. Adv.* **4** eaar5313
[75] Tielrooij K J *et al* 2018 Out-of-plane heat transfer in van der Waals stacks through electron–hyperbolic phonon coupling *Nat. Nanotechnol.* **13** 41–6
[76] Baudin E, Voisin C and Placais B 2020 Hyperbolic phonon polariton electroluminescence as an electronic cooling pathway *Adv. Funct. Mater.* **30** 1904783
[77] Brida D *et al* 2013 Ultrafast collinear scattering and carrier multiplication in graphene *Nat. Commun.* **4** 1987
[78] Rana F, George P A, Strait J H, Dawlaty J, Shivaraman S, Chandrashekhar M and Spencer M G 2009 Carrier recombination and generation rates for intravalley and intervalley phonon scattering in graphene *Phys. Rev.* B **79** 115447
[79] Wang H *et al* 2010 Ultrafast relaxation dynamics of hot optical phonons in graphene *Appl. Phys. Lett.* **96** 081917
[80] Grosso G and Pastori Parravicini G 2013 *Solid State Physics* (New York: Academic)
[81] Marini A, Cox J D and De Abajo F J G 2017 Theory of graphene saturable absorption *Phys. Rev.* B **95** 125408